ChemComm

COMMUNICATION

View Article Online
View Journal | View Issue

Cite this: *Chem. Commun.*, 2025, **61**, 15175

Received 23rd July 2025,
Accepted 26th August 2025

DOI: 10.1039/d5cc04187b

rsc.li/chemcomm

Transfer-free growth of wafer-level graphene *via* a Mo sacrificer

Wenze Wei,†[ab] Yiming Luo,†[c] Kaixuan Zhou,*[b] Yaqi Gao,[d] Feifan Liu,[ab] Shihao Zhu,[c] Tongbo Wei,[d] Li Jia,*[b] Zhongfan Liu[b] and Jingyu Sun*[ab]

This study presents a straightforward method to allow transfer-free graphene growth on SiO_2/Si substrates, with Mo serving as a sacrificial layer, which could be easily removed by simple air blowing. Such a route eliminates the need for chemical etching of metal catalysts. The resulting 2-inch graphene wafer shows electrical uniformity and minimal metal residue.

Since graphene was first successfully exfoliated by Novoselov *et al.* in 2004,[1] it has been extensively studied as a two-dimensional material with many attractive properties, such as high transparency,[2] excellent carrier mobility,[3] and favorable mechanical robustness.[4] In this sense, graphene films on insulating substrates hold significant potential for applications in the fabrication of field-effect transistors, light-emitting diodes and photovoltaic devices.[5–7]

Among the explored methods for graphene preparation, chemical vapor deposition (CVD) has emerged as a reliable route for producing high-quality graphene films because of its exceptional controllability and scalability. In general, there are several main CVD strategies aimed at synthesizing graphene over insulators towards electronic/optoelectronic devices:[8–10] (i) the direct growth on a target insulating substrate, (ii) the catalytic growth on metal films followed by transfer onto a target insulating substrate, and (iii) the interfacial growth on a target insulator by the introduction of a sacrificial metal layer, which could be etched away afterwards. Nevertheless, owing to the catalytic inertness and carbon migration difficulty of insulators, daunting challenges remain in the direct growth of graphene, which typically results in poor growth quality, limited controllability, and small domain sizes.[11–15] The metal-assisted route has been proven as an effective strategy in facilitating precursor decomposition, reducing the migration barrier of active carbon species and improving the growth quality. For instance, wafer-scale single-crystal graphene was synthesized on Cu(111) by carefully controlling the annealing step of the substrate.[16] In addition, high-quality graphene can be produced by depositing a Ni or Cu/Ni alloying layer, which allowed carbon atoms to dissolve into the bulk of the catalyst.[17,18] Upon cooling, supersaturated carbon precipitates at the interface between Ni and the insulating substrate, forming a graphene film. Despite the enhancement in the graphene quality, removing the catalytic metal layer and/or transferring the graphene after growth is tedious and problematic. Any metallic or organic residues would further impact the ultimate properties of the thus-obtained graphene.[19]

Inspired by these considerations, we propose herein an innovative transfer-free graphene growth method by utilizing Mo as a growth booster, which could be easily removed by air blowing. This approach eliminates the need for post chemical processing to remove the metal layer or transfer the produced graphene. The resulting graphene film on the 2-inch SiO_2/Si wafer exhibits excellent uniformity, with no detectable metallic residues as confirmed by elemental analysis.

Fig. 1a schematically depicts the transfer-free growth of graphene. Briefly, a Mo layer with a thickness of ~200 nm was sputtered onto the SiO_2/Si substrate, followed by the oxidation to MoO_3 in air at 350 °C. The MoO_3 layer was then carbonized at 900 °C in a methane-rich atmosphere. By further increasing the system temperature to 1080 °C while reducing the methane concentration, the graphene growth could be initiated. After cooling down to room temperature, the coverage layer was completely removed using N_2 or air gas blowing (Fig. S1, S2 and Movie S1). Fig. 1b shows a photograph of a 2-inch SiO_2/Si wafer before (left panel) and after (right panel) graphene preparation with Mo deposition. Upon air blowing, no noticeable metallic residues were visible over the surface

[a] *College of Energy, Soochow Institute for Energy and Materials Innovations, SUDA-BGI Collaborative Innovation Center, Jiangsu Provincial Key Laboratory for Advanced Carbon Materials and Wearable Energy Technologies, Soochow University, Suzhou 215006, China. E-mail: sunjy86@suda.edu.cn*
[b] *Beijing Graphene Institute, Beijing 100095, China. E-mail: zhoukx@bgi-graphene.com, jiali@bgi-graphene.com*
[c] *College of Advanced Interdisciplinary Studies, National University of Defense Technology, Changsha 410073, China*
[d] *Institute of Semiconductors, Chinese Academy of Sciences, Beijing 100083, China*
† Wenze Wei and Yiming Luo contributed equally.

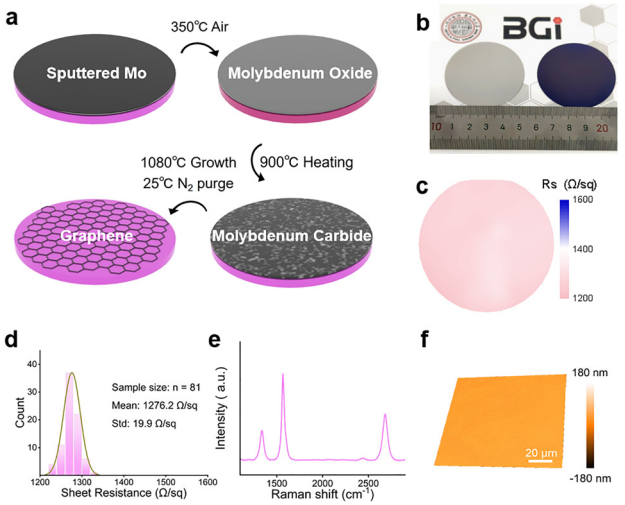

Fig. 1 (a) Schematic of the graphene preparation process. (b) Photograph of a 2-inch wafer with 200 nm Mo sputtered (left) and few-layer graphene grown (right) after air blow treatment. (c) Sheet resistance map. (d) Sheet resistance statistical data. (e) Raman spectra and (f) white light interferometer characterisation of the as-grown graphene.

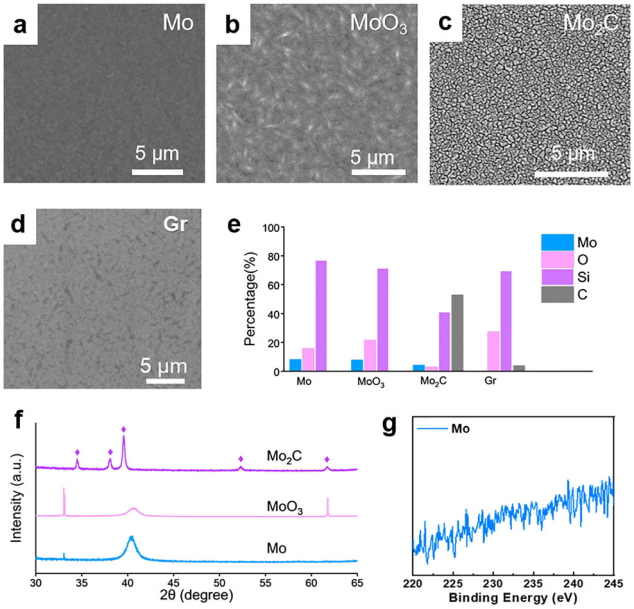

Fig. 2 SEM images of the substrate after (a) Mo sputtering, (b) oxidation, (c) carburization, and (d) graphene growth. (e) Elemental composition at each stage examined by EDS analysis. (f) XRD patterns of the substrate at each preparation stage. (g) XPS Mo 3d spectrum of the as-prepared graphene.

across its entire wafer area. Fig. 1c and 1d present the sheet resistance mapping and related statistical data for the prepared graphene. The average sheet resistance of the measured 81 points reaches 1276 Ω sq^{-1} with a standard deviation of 19.9 Ω sq^{-1}, demonstrating the wafer-scale uniformity of the graphene. As displayed in Fig. 1e, a representative Raman spectrum of the produced graphene film exhibits an I_D/I_G ratio of 0.34 and an I_{2D}/I_G ratio of 0.53. The full width at half maximum (FWHM) of the 2D peak is 68.4 cm^{-1}. And these results suggest the few-layer graphene formation.[20,21] Atomic force microscopy measurements were performed to further evaluate the layer numbers of the graphene film. A trench with a depth of nearly 2.8 nm was observed (Fig. S3), indicating that the graphene film comprises *ca.* 8 layers.[22] The white light interferometer measurement of graphene over the 112 × 112 μm^2 area shows a surface roughness of 0.59 nm (Fig. 1f).

A varied characterisation toolbox was employed to identify the content of the Mo-based catalyst layer at each preparation stage. In the initial stage after Mo sputtering, the surface morphology of the substrate showcases uniformly fine particle aggregation, as evidenced by the scanning electron microscopy (SEM) image in Fig. 2a. The corresponding X-ray diffraction (XRD) pattern manifests two prominent signals at 33.1° and 40.5° (blue curve, Fig. 2f). The strong peak at 40.5° corresponds to Mo(110) (JCPDS 89-5023). Note that its FWHM exceeds 1°, indicative of internal stress in the sputtered Mo layer. The peak at 33.1° is likely owing to the surface oxidation to MoO_3 when exposed to air.[23] As shown in Fig. S4, the corresponding Raman peak at 995 cm^{-1} could be ascribed to MoO_3.[24,25] The energy-dispersive spectroscopy (EDS) results confirm the presence of Mo and O elements (Fig. S5). Upon 350 °C oxidation treatment, the surface morphology of the Mo layer presents noticeable bulging (Fig. 2b). The XRD pattern respectively shows a marked increase/decrease in the peak intensity of MoO_3/Mo (pink curve, Fig. 2f). The Raman peak at 995 cm^{-1} becomes relatively stronger compared to that in the previous stage, indicating further oxidation into MoO_3.

After carburization at 900 °C, the substrate surface manifests a cracking morphology with discernible gaps between the grains (Fig. 2c). The diffraction pattern of the carbonized sample matches well with hexagonal β-Mo_2C (JCPDS 35-0787), affording featured signals at 34.4° (100), 38.1° (002), 39.4° (101), 52.2° (102), and 61.5° (110) (purple curve, Fig. 2f). According to the EDS analysis, the atomic composition of Mo, O and C element, respectively, reaches 4.0%, 2.7% and 52.5%, indicating that the majority of MoO_3 transformed to Mo_2C in this stage (Fig. 2e). After graphene formation, the surface is covered by a uniform film (Fig. 2d), where the EDS analysis shows no sign of Mo element (Fig. 2e). To further probe the purity of graphene prepared by our method, X-ray photoelectron spectroscopy (XPS) and inductively coupled plasma mass spectrometry (ICP-MS) were employed. The high-resolution Mo 3d XPS spectra display no obvious signals; the ICP-MS results also reveal a Mo content of less than 0.002%, implying that the obtained graphene is free of Mo residues (Fig. 2g and Fig. S6).

It is interesting to find that the processing duration of the carburization stage determines the difficulty level with respect to Mo sacrificial layer removal. To investigate the removal essence, the Mo oxidation and graphene growth parameters were kept identical, with varied carburization duration set at 5, 10 or 20 min for comparison. The resulting samples were characterised by optical microscopy (Fig. S7). In terms of the carburization for 5 min, the pre-deposited Mo layer could not be detached from the substrate surface using air blowing. As for

the sample carburized for 10 min, parts of the layer were removed. In contrast, for the sample carburized for 20 min, complete layer removal could be realized. Moreover, surface cracking textures were observed for all carburization cases, with related traces remaining in the graphene films. Raman spectra collected specifically in the grain (light-coloured) and grain boundary (dark-coloured) regions, respectively, manifest the I_{2D}/I_G ratio at 0.4 and 0.19 (Fig. S8), suggesting that the grown graphene is apparently thicker at the grain boundaries as compared to that at the grains. It is also worth-noting that the I_D/I_G ratios differ significantly between the two regions. A possible explanation is that the substrate beneath the grain boundaries is directly exposed to the gas-phase environment, whereas the substrate beneath the grain regions represents a confined growth system, in which a confined space is formed between Mo_2C and the substrate. Such a regional difference might alter the graphene growth mode, resulting in disparities in both thickness and defect density.[26]

Such a phenomenon might be attributed to the diffusion of active carbon species through the grain boundaries of the formed Mo_2C, as schematically depicted in Fig. 3a. As the carburization progresses, the gradually boosted number of grain boundaries readily creates migration pathways for the active carbon species, allowing graphene to deposit onto the SiO_2/Si substrate. It is worth-noting that the carburization of Mo typically precedes the growth of graphene because of the strong affinity between Mo and carbon. After the formation of Mo_2C, the growth of graphene begins to occur.[27]

In comparison with the conventional post-treatment routes of CVD-grown graphene such as film transfer and/or chemical etching, the metal removal approach developed in this work offers certain advantages in both operational simplicity and processing speed. In detail, previously reported methods for multilayer graphene synthesis using metal catalysts with post-processing durations are summarized (Table S1). It is evident that the etching-based metal removal procedures normally require immersion in etchants for hours and additional transfer processes, whereas our air blowing method enables complete removal within 60 s. To gain insight into the ease-of-removal feature of carburized Mo, density functional theory (DFT) calculations were carried out to quantify the interfacial binding strength in the system. As presented in Fig. 3b, the calculated binding energy between graphene and Mo_2C is 2.15 eV, which is 30% of that between MoO_3 and SiO_2, as well as 40% of that between graphene and SiO_2. The relatively weak binding energy between graphene and Mo_2C facilitates its separation without detaching the graphene from the SiO_2 substrate. In contrast, the binding energy value between MoO_3 and SiO_2, as well as between Mo and SiO_2, reaches 7.3 and 7.9 eV, respectively (calculation details available in the SI). Such a strong binding strength accounts for the incompetence to fully remove the Mo-based sacrificial layer prior to complete carburization.

To evaluate the optoelectronic application potential of the as-produced graphene/Si material, a GaN-based photodetector was constructed. The optical response of the graphene-based GaN metal–semiconductor–metal (MSM) photodetector under a 400 nm photo-illumination is shown in Fig. 4a. In the absence of illumination, the dark current increases from 0.29 to 15.8 nA as the applied bias voltage is increased from 5 to 20 V. The corresponding photocurrent increases from 1.46 to 42.5 nA. These results indicate a stable and reproducible photoresponse behaviour. Fig. 4b shows the time-resolved photocurrent of the photodetector in response to the turn-on and turn-off of 400 nm photo-illumination (5.31 μW cm^{-2}), demonstrating the capability of detecting the light signals. Note that the responsivity (R) and specific detectivity (D^*) are important metrics for quantifying the performance of photodetectors.[28] Among them, R is a parameter that describes the sensitivity of a photodetector, reflecting its ability to convert an optical signal into an electrical signal, as characterised by the relationship between the output signal of the photodetector and the input

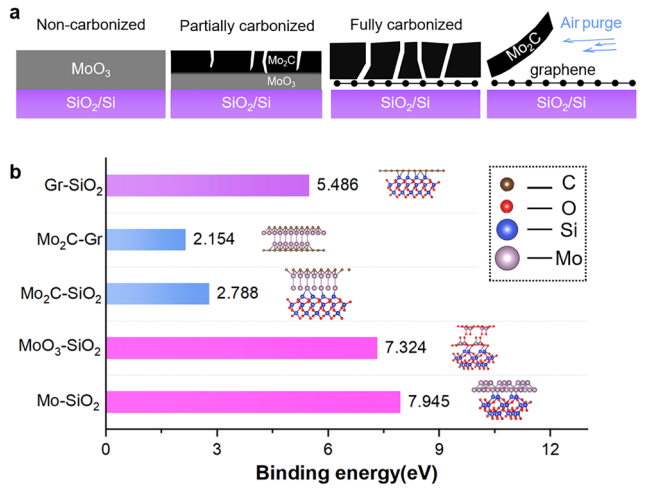

Fig. 3 (a) Schematic of graphene growth and Mo sacrificial layer removal. (b) DFT calculation results of the binding energy between the graphene-SiO_2, Mo_2C-graphene, Mo_2C-SiO_2, MoO_3-SiO_2, and Mo-SiO_2 interfaces.

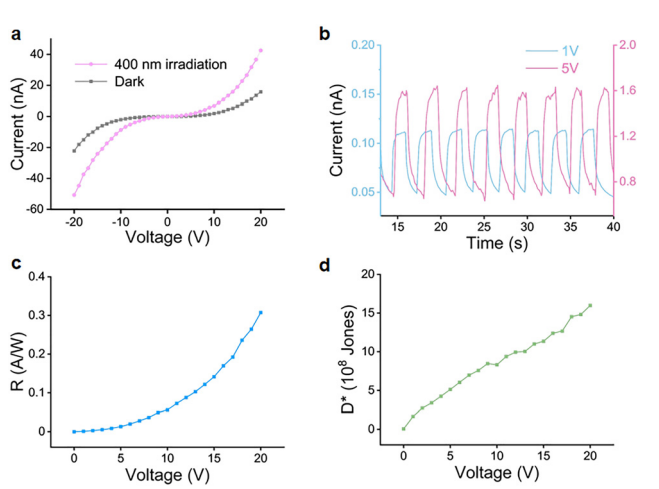

Fig. 4 (a) I–V and (b) I–t profiles of the GaN-based MSM photodetector under 400 nm photo-illumination. (c) The R and (d) D^* plot as a function of applied bias voltage.

radiation. The R here could be calculated using the equation:

$$R = \frac{I_{ph} - I_{dark}}{P_\lambda \cdot A}$$

where I_{ph} and I_{dark} are the photocurrent and dark current, respectively, P_λ is the incident light power density (0.0531 W m^{-2}), λ is the wavelength of incident light (400 nm) and A is the effective area of the photodetector (0.0137 cm^2). As shown in Fig. 4c, the R increases from 0.87 μA W^{-1} to 0.307 A W^{-1} with an increasing bias voltage up to 20 V, and the exponential increase in responsivity with the bias voltage confirms favourable photo-response performance.[29] As another core indicator, specific detectivity (D^*) describes the ability to detect light in the presence of noise, which could be calculated by:

$$D^* = \frac{\sqrt{A}R}{\sqrt{2eI_{dark}}}$$

where e is the elementary charge. Our photodetector exhibits a D^* value of 1.6×10^9 Jones at 20 V (Fig. 4d).

In conclusion, we present a clean and transfer-free strategy for the growth of uniform few-layer graphene on SiO_2/Si substrates using a Mo sacrificial layer. In contrast to the prevailing Cu- or Ni-involved routes, the Mo-base layer could be completely removed by an air-blowing process, eliminating the need for post-treatment such as chemical etching. The resulting graphene film shows no detectable metallic residues and exhibits excellent uniformity with low surface roughness. In combination with instrumental characterisations and DFT calculations, we reveal that Mo transforms to Mo_2C during the carburization, enabling graphene growth and facilitating subsequent catalyst removal. Our method significantly reduces contamination risks and offers promising potential for scalable integration of graphene-based optoelectronic devices.

The financial support for this work was provided by the National Natural Science Foundation of China (T2188101 and 22179089) and the National Key Research & Development Program of China (2019YFA0708201).

Conflicts of interest

There are no conflicts to declare.

Data availability

The data supporting this article have been included as part of the SI. Supplementary information: Supplementary methods and additional characterisations of graphene. See DOI: https://doi.org/10.1039/d5cc04187b

References

1 K. S. Novoselov, A. K. Geim, S. V. Morozov, D. Jiang, Y. Zhang, S. V. Dubonos, I. V. Grigorieva and A. A. Firsov, *Science*, 2004, **306**, 666–669.
2 R. R. Nair, P. Blake, A. N. Grigorenko, K. S. Novoselov, T. J. Booth, T. Stauber, N. M. R. Peres and A. K. Geim, *Science*, 2008, **320**, 1308.
3 X. Du, I. Skachko, A. Barker and E. Y. Andrei, *Nat. Nanotechnol.*, 2008, **3**, 491–495.
4 C. Lee, X. Wei, J. W. Kysar and J. Hone, *Science*, 2008, **321**, 385–388.
5 X. Wang and G. Shi, *Energy Environ. Sci.*, 2015, **8**, 790–823.
6 F. Zhang, K. Yang, G. Liu, Y. Chen, M. Wang, S. Li and R. Li, *Composites, Part A*, 2022, **160**, 107051.
7 J. Kim, C. Bayram, H. Park, C.-W. Cheng, C. Dimitrakopoulos, J. A. Ott, K. B. Reuter, S. W. Bedell and D. K. Sadana, *Nat. Commun.*, 2014, **5**, 4836.
8 B. Jiang, S. Wang, J. Sun and Z. Liu, *Small*, 2021, **17**, 2008017.
9 K. S. Novoselov, V. I. Fal′ko, L. Colombo, P. R. Gellert, M. G. Schwab and K. Kim, *Nature*, 2012, **490**, 192–200.
10 J. Zhang, L. Sun, K. Jia, X. Liu, T. Cheng, H. Peng, L. Lin and Z. Liu, *ACS Nano*, 2020, **14**, 10796–10803.
11 H. Wang, X. Xue, Q. Jiang, Y. Wang, D. Geng, L. Cai, L. Wang, Z. Xu and G. Yu, *J. Am. Chem. Soc.*, 2019, **141**, 11004–11008.
12 K. Jia, J. Zhang, L. Lin, Z. Li, J. Gao, L. Sun, R. Xue, J. Li, N. Kang, Z. Luo, M. H. Rummeli, H. Peng and Z. Liu, *J. Am. Chem. Soc.*, 2019, **141**, 7670–7674.
13 S. Wei, L.-P. Ma, M.-L. Chen, Z. Liu, W. Ma, D.-M. Sun, H.-M. Cheng and W. Ren, *Carbon*, 2019, **148**, 241–248.
14 H. Wang and G. Yu, *Adv. Mater.*, 2016, **28**, 4956–4975.
15 R. Liu, Z. Peng, X. Sun, Z. Chen, Z. Li, H. Ci, B. Liu, Y. Cheng, B. Jiang, J. Hu, W. Yin, J. Sun and Z. Liu, *Nano Res.*, 2023, **16**, 6334–6342.
16 Y. Zhu, J. Zhang, T. Cheng, J. Tang, H. Duan, Z. Hu, J. Shao, S. Wang, M. Wei, H. Wu, A. Li, S. Li, O. Balci, S. M. Shinde, H. Ramezani, L. Wang, L. Lin, A. C. Ferrari, B. I. Yakobson, H. Peng, K. Jia and Z. Liu, *Adv. Mater.*, 2024, **36**, 2308802.
17 M. Wang, M. Huang, D. Luo, Y. Li, M. Choe, W. K. Seong, M. Kim, S. Jin, M. Wang, S. Chatterjee, Y. Kwon, Z. Lee and R. S. Ruoff, *Nature*, 2021, **596**, 519–524.
18 W. Qiu, Y. Guo, Q. Zhang, J. Hu, J. Peng, Y. Hu, D. Chen, C. Yang, P. Li and M. Pan, *ACS Appl. Nano Mater.*, 2023, **6**, 4236–4242.
19 L. Lin, J. Zhang, H. Su, J. Li, L. Sun, Z. Wang, F. Xu, C. Liu, S. Lopatin, Y. Zhu, K. Jia, S. Chen, D. Rui, J. Sun, R. Xue, P. Gao, N. Kang, Y. Han, H. Q. Xu, Y. Cao, K. S. Novoselov, Z. Tian, B. Ren, H. Peng and Z. Liu, *Nat. Commun.*, 2019, **10**, 1912.
20 L. M. Malard, M. A. Pimenta, G. Dresselhaus and M. S. Dresselhaus, *Phys. Rep.*, 2009, **473**, 51–87.
21 Z. Ni, Y. Wang, T. Yu and Z. Shen, *Nano Res.*, 2008, **1**, 273–291.
22 G. Eda, G. Fanchini and M. Chhowalla, *Nat. Nanotechnol.*, 2008, **3**, 270–274.
23 P. Chelvanathan, K. S. Rahman, M. I. Hossain, H. Rashid, N. Samsudin, S. N. Mustafa, B. Bais, M. Akhtaruzzaman and N. Amin, *Thin Solid Films*, 2017, **621**, 240–246.
24 S. Patnaik, G. Swain and K. M. Parida, *Nanoscale*, 2018, **10**, 5950–5964.
25 M. Dieterle, G. Weinberg and G. Mestl, *Phys. Chem. Chem. Phys.*, 2002, **4**, 812–821.
26 J. Pang, R. G. Mendes, P. S. Wrobel, M. D. Wlodarski, H. Q. Ta, L. Zhao, L. Giebeler, B. Trzebicka, T. Gemming, L. Fu, Z. Liu, J. Eckert, A. Bachmatiuk and M. H. Rümmeli, *ACS Nano*, 2017, **11**, 1946–1956.
27 Z. Zou, L. Fu, X. Song, Y. Zhang and Z. Liu, *Nano Lett.*, 2014, **14**, 3832–3839.
28 Y. Long, K. Ba, J. Liu, X. Deng, Y. Di, K. Xiong, Y. Chen, X. Wang, C. Liu, Z. Li, D. Liu, X. Fang, Q. Liu and J. Wang, *Mater. Today Electron.*, 2024, **10**, 100116.
29 Y. Gao, J. Yang, X. Ji, R. He, J. Yan, J. Wang and T. Wei, *ACS Appl. Mater. Interfaces*, 2022, **14**, 21232–21241.

